

# Three-Dimensional and Selective Displacement Sensing of a Levitated Nanoparticle via Spatial Mode Decomposition

Thomas J. Dinter<sup>1,\*</sup>, Reece Roberts<sup>1,2</sup>, Thomas Volz<sup>1,2</sup>, Mikołaj K. Schmidt<sup>1,2</sup>, and Cyril Laplane<sup>1,2,3†</sup>

<sup>1</sup> *School of Mathematical and Physical Sciences, Macquarie University, NSW 2109, Australia*

<sup>2</sup> *ARC Centre for Engineered Quantum Systems (EQUS), Macquarie University, NSW 2109, Australia and*

<sup>3</sup> *Sydney Quantum Academy, Sydney, NSW 2006, Australia*

(Dated: November 6, 2024)

We propose and experimentally demonstrate a novel detection method that significantly improves the precision of real-time measurement of the three-dimensional displacement of a levitated dipolar scatterer. Our technique relies on the spatial mode decomposition of the light scattered by the levitated object, allowing us to simultaneously and selectively extract the position information of all translational degrees of freedom with minimal losses. To this end, we collect all the light back-scattered from a levitated nanoparticle using a parabolic mirror and couple it into a spatial mode sorter. The sorter effectively demultiplexes the information content of the scattered electric field, resulting in each of the nanoparticle's translational degrees of freedom being selectively encoded in the amplitude of orthogonal optical modes. We report measurement efficiencies of  $(\eta_{\text{tot}}^x, \eta_{\text{tot}}^y, \eta_{\text{tot}}^z) = (0.14, 0.16, 0.32) > 1/9$ , which should enable the 3D motional quantum ground state of a levitated optomechanical system. Further, we believe this technique opens up the possibility to implement coherent feedback control of a levitated nanoparticle.

Levitated optomechanical systems have recently entered the quantum regime, with several demonstrations having now achieved cooling to the center-of-mass (COM) motional quantum ground state [1–4]. Such platforms present an exciting avenue for designing tests of fundamental physics [5–8], and in particular for matter-wave interferometry experiments with mesoscopic objects [9] several orders of magnitude larger than the current state-of-the-art [10, 11]. A common prerequisite for most of these proposals is to prepare the levitated mechanical oscillator in its motional quantum ground state. To achieve ground-state cooling, research efforts can be separated into two distinct approaches: passive cooling using coherent scattering in a cavity [1, 12, 13], and active cooling with measurement-based control techniques [2, 3]. In particular, the latter actively controls an object's mechanical motion by applying a position or velocity-dependent feedback force. Hence, measurement-based control techniques are highly dependent on the efficiency with which we can collect information on the system's dynamics.

It was recently understood that information on the different motional degrees of freedom (DOFs) are encoded in specific spatial radiation patterns, so-called *information radiation patterns* [14, 15]. Because of this non-uniformity, it is a difficult task to construct a detection system capable of efficiently and simultaneously measuring each motional DOF of a levitated nanoparticle. In particular, this requires either a carefully engineered local oscillator to optimally interfere with the scattered light

[16] or position-sensitive detectors (such as a quadrant photodiode) that are blind to specific DOFs. The latter approach would intrinsically require beam-splitting, introducing extensive optical losses. As a result, so far, conventional interferometric techniques have only been able to reach quantum-enabling measurement efficiencies for the motion parallel to the propagation axis of the optical tweezer [2–4], often at the detriment of the transverse translational DOFs.

In this work, we present a novel approach to displacement sensing that relies on decomposing the light scattered from a levitated nanoparticle in the appropriate basis of spatial modes. This allows us to passively and efficiently isolate contributions from all three translational DOFs without the need for direct measurement. This kind of filtering, which utilises properties of the scattered electric field rather than the scattered power, preserves the coherence of the collected light. Consequently, it holds promise for use in all-optical coherent feedback control schemes, which avoid the decoherence and back-action associated with a quantum measurement [17–19]. As a convenient demonstration of our method, we choose the linearly polarised (LP) mode basis of an optical fiber, encoding information on each translational DOF in the amplitude of a unique LP mode. The experimental setup relies on simple, telecommunication grade and commercially available components, providing a path towards a compact and fully integrated levitated optomechanical platform. Finally, we perform parametric feedback cooling [20], achieving temperatures of  $(T_x, T_y, T_z) = (7, 100, 20)$  mK at pressures of  $5 \times 10^{-5}$  mbar, and show that our detection technique allows us to reach the measurement efficiencies necessary for realizing the 3D motional quantum ground state of a levitated nanoparticle.

We consider the case of a sub-wavelength nanoparti-

\* thomas.dinter@hdr.mq.edu.au

† cyril.laplane@sydney.edu.au;

Present address: School of Physics, The University of Sydney, NSW 2006, Australia

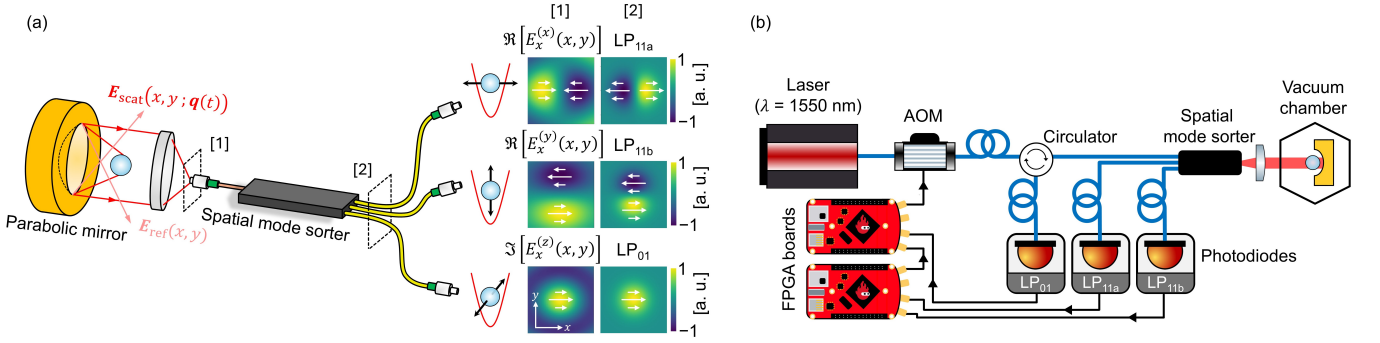


FIG. 1. **(a)** The operating principle of our displacement sensing technique using a spatial mode sorter. In the focal plane of the collection lens, labelled [1], the scattered field and reference field are coupled into the few-mode optical fiber input of the device. In the panel [1] on the right, we show the dominant components of the inelastically scattered field  $E_x^{(q)}(x, y)$ , which carries information on the nanoparticle's motion along the  $\hat{e}_q$  axis, and couples predominantly to a single LP mode. In the output plane, labelled [2], information on each translational degree of freedom  $q(t)$  is stored in a unique channel of the sorter (see panel [2] on the right for the plots of the electric fields of the three fiber modes). **(b)** The output of a  $\lambda = 1550$  nm laser is controlled by an acousto-optic modulator (AOM) and coupled into the LP<sub>01</sub> channel of a space-division demultiplexing photonic chip, producing a 100 mW optical tweezer at the focus of a high numerical aperture parabolic mirror. The back-scattered light from a levitated nanoparticle is then coupled back into the photonic chip, allowing us to measure each translational degree of freedom independently.

cle, which is well-approximated as an isotropic dipolar scatterer, confined to the focus of a linearly ( $x$ ) polarised trapping beam. In particular, we model the geometry shown in Fig. 1(a), where the trapping beam is focused by a high-numerical aperture (NA) parabolic mirror. This implementation presents a key advantage over traditional setups [21], in that it collects all of the back-scattered light, which is collimated and subsequently coupled into a few-mode optical fiber in the focal plane of a collection lens. At the output of the few-mode fiber, we measure the recovered power to extract information on the nanoparticle's real time position.

In the limit of small displacements, we can write the scattered field in the focal plane of the collection lens as a sum of elastically and inelastically scattered light (see Supplementary Material, Appendix A). In particular, we find that only the inelastically scattered light is modulated by the nanoparticle's real time position and thus is the only one to contribute meaningfully to the measurement result. To first order, we approximate the scattered field as

$$\mathbf{E}_{\text{scat}}(x, y; \mathbf{q}(t)) = \overbrace{\mathbf{E}_0(x, y)}^{\text{elastic}} + \sum_{q=x,y,z} \frac{q(t)}{w_0} \overbrace{\mathbf{E}^{(q)}(x, y)}^{\text{inelastic}}, \quad (1)$$

where  $w_0$  refers to the trapping beam waist at the focus of the parabolic mirror, and  $q(t)$  refers to the nanoparticle's position along the  $\hat{e}_q$  axis. In addition to these terms, we must also consider the unscattered and diverging part of the trapping beam,  $\mathbf{E}_{\text{ref}}(x, y)$ , which functions as the local oscillator (LO) in the simplest conventional interferometry-based detection systems. In the focal plane of the collection lens, this field is well-approximated by a plane wave and can usually be tuned such that  $|\mathbf{E}_{\text{ref}}(x, y)| \gtrsim |\mathbf{E}_{\text{scat}}(x, y; \mathbf{q}(t))|$ .

In Fig. 1(a) we compare the dominant polarisation component of the inelastically scattered field  $\mathbf{E}^{(q)}(x, y)$  to the lowest-order LP modes. We find that displacements parallel to the trapping axis ( $\hat{e}_z$ ) produce an electric field profile reminiscent of the LP<sub>01</sub> mode supported on optical fibers. Conversely, the fields produced for displacements along  $\hat{e}_x$  and  $\hat{e}_y$  are reminiscent of the LP<sub>11a</sub> and LP<sub>11b</sub> modes, respectively. Inspired by this observation, we have opted to couple the scattered field into a space-division demultiplexing photonic chip [22], which functions as a spatial mode sorter. As depicted schematically in Fig. 1(a), this allows us to isolate contributions from each translational DOF in amplitude modulations of a unique LP mode. Before quantifying this effect, however, let us first consider the experimental setup used to implement this selective measurement protocol.

We optically levitate spherical SiO<sub>2</sub> nanoparticles of diameter 310 nm, using the experimental setup illustrated in Fig. 1(b). We load the trap at ambient pressure using an ultrasonic nebulizer and a dilute solution of sonicated SiO<sub>2</sub> suspended in ethanol. The trapping beam is tuned to a wavelength of  $\lambda = 1550$  nm and set to a power of approximately 100 mW. Upon loading the optical trap, the system is decompressed in a two stage pumping process to a vacuum on the order of  $5 \times 10^{-5}$  mbar.

In the focal plane of the collection lens, the scattered field is coupled into the spatial mode sorter [22]. The input is a few-mode, graded-index optical fiber with a core diameter of approximately 8  $\mu\text{m}$ , supporting the LP<sub>01</sub>, LP<sub>11a</sub> and LP<sub>11b</sub> modes. Once excited, the electric field associated with each of these modes is transferred to a unique single-mode output fiber using a tapered mode-selective coupler [23, 24]. Each output channel is then sent to a low-noise photodiode, with a typical set of detected signals shown in Fig. 2. For an  $x$ -

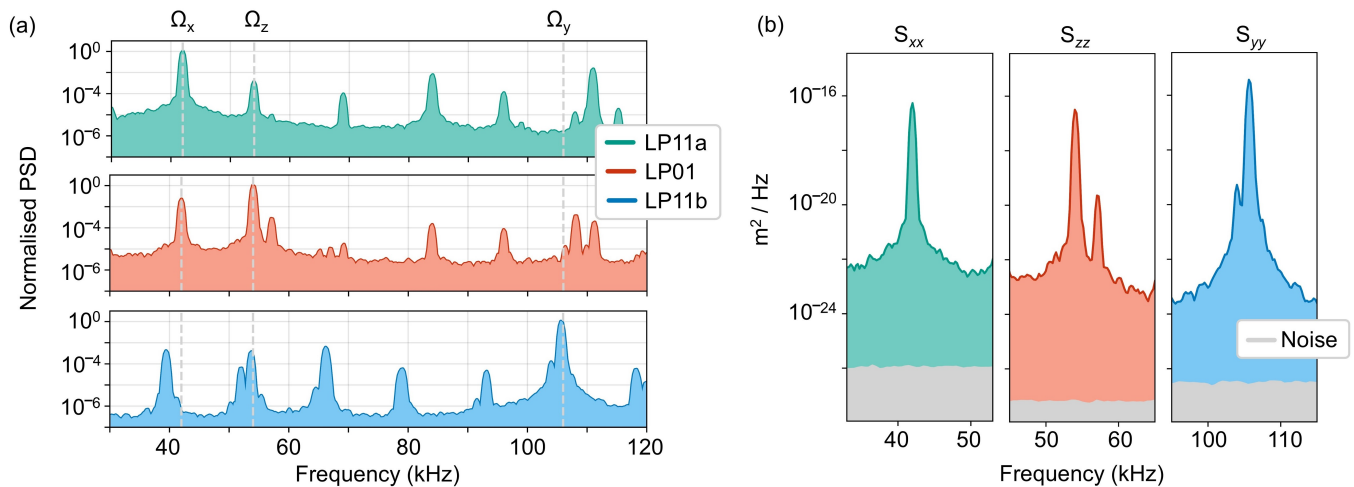


FIG. 2. (a) Measured power spectral densities (PSDs) at the LP<sub>01</sub>, LP<sub>11a</sub> and LP<sub>11b</sub> output channels of the spatial mode sorter, normalised to the highest contribution in each channel. Note that each channel has contributions from primarily a translational degree of freedom, as predicted from the profile of  $\mathbf{E}^{(q)}(x, y)$ . (b) Calibrated PSDs, restricted to only a single  $S_{qq}(\Omega)$  for  $q = x, y$  and  $z$ . The shot noise floor is also shown (grey).

polarized trapping beam, we observe oscillation frequencies  $(\Omega_x, \Omega_y, \Omega_z) / 2\pi \approx (42, 106, 54)$  kHz for each translational DOF. The other spurious spectral features in Fig. 2(a) are a consequence of the large nanoparticles used here, which experience coupling between different translational DOFs at room temperature (300 K) [25]. This leads to the generation of spectral features at frequencies given by various linear combinations of  $\Omega_x$ ,  $\Omega_y$ , and  $\Omega_z$  [26].

For parametric feedback cooling, the signal of each photodiode is sent to an FPGA board, which functions as a digital phase-locked loop (PLL), with the recovered signal filtered and phase-shifted to generate a feedback signal at twice the natural oscillation frequency  $2\Omega_q$ . These feedback signals are used to modulate the power of the trapping beam via an acousto-optic modulator (AOM).

In Fig. 2(a) we plot the power spectral densities (PSDs) of the signals measured at each output channel of the spatial mode sorter. We find that each output channel contains information on primarily a single translational DOF, equivalent to the nanoparticle's motion along a particular spatial axis, encoded in  $S_{qq}(\Omega)$  for  $q = x, y$  and  $z$ . In particular, we observe good extinction ratios on the order of approximately 20 dB, with the dominant spectral feature in each output channel being at least two orders of magnitude larger than all others. We plot these features, marking the shot noise floor for each output channel, in Fig. 2(b). These extinction ratios match the technical specification supplied for the spatial mode sorter for the LP<sub>11a</sub> and LP<sub>11b</sub> channels, suggesting that we may be limited by the performance capabilities of the device.

To quantify, and better understand the extent and limitations of this selectivity, we have numerically modelled the coupling efficiency of the scattered fields to each LP

mode, defined as the spatial overlap integral

$$\eta_q^{\ell,m} = \frac{\left| \iint [\mathbf{E}^{(q)}(x, y)]^* \cdot \mathbf{LP}_{\ell,m}(x, y) \, dx dy \right|}{\sqrt{\iint |\mathbf{E}^{(q)}(x, y)|^2 \, dx dy \iint |\mathbf{LP}_{\ell,m}(x, y)|^2 \, dx dy}}, \quad (2)$$

where  $\mathbf{LP}_{\ell,m}(x, y)$  refers to the electric field of the LP <sub>$\ell,m$</sub>  mode, and integration is performed over the end-face of the input optical fiber. This procedure, including the corrections made to account for the geometry of our setup, can be found in Appendix B (see Supplementary Material). Finally, note that we can write down analogous expressions for the coupling of the elastically scattered and LO fields also. The coefficients calculated for the particular experimental setup used here are reported in Fig. 3, with a detailed discussion on how we expect these quantities to relate to the measured PSDs found in Appendix D.

The results shown in Fig. 3 qualitatively agree with the experimental results, with the LP<sub>11a</sub> (LP<sub>11b</sub>) mode coupling predominantly to the inelastically scattered field generated by displacements along  $\hat{e}_x$  ( $\hat{e}_y$ ), and the LP<sub>01</sub> mode containing only weak contributions from both the transverse DOFs. Interestingly, the elastically scattered and LO fields are only weakly coupled to the LP<sub>11a/b</sub> modes, due to their spatial asymmetry. This would typically be disadvantageous in conventional detection systems, which rely on the LO to extract information from the phase of the scattered light. However, due to the coherent nature of the coupling described in Eq. (2), this is not the case in our approach. Indeed, any phase or amplitude modulation of the input field is naturally transformed to amplitude modulation of the LP modes upon coupling into the spatial mode sorter.

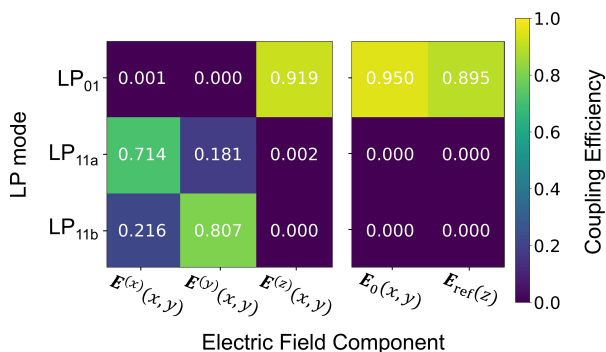


FIG. 3. The coupling efficiency of each electric field component to each LP mode supported by the spatial mode sorter, in the focal plane of the collections lens. We find that the inelastically scattered field components,  $\mathbf{E}^{(q)}(x, y)$ , selectively couple to specific LP modes. Note that the LP<sub>11a/b</sub> modes are effectively de-coupled from the elastically scattered and LO fields,  $\mathbf{E}_0(x, y)$  and  $\mathbf{E}_{ref}(x, y)$ , respectively.

That is not to say that the decoupling of the LP<sub>11a/b</sub> modes from the LO field is inconsequential. Indeed, we find that in the absence of the LO field the measurement imprecision reduces to a much simpler form. This form is derived in Appendix C (see Supplementary Material) where we show that

$$S_{imp,q}^{\ell,m} = \frac{\hbar kc}{8\pi} \sqrt{\frac{\mu_0}{\epsilon_0}} \frac{1}{\alpha_q^2} \frac{w_0^2}{(\eta_q^{\ell,m})^2}, \quad (3)$$

where  $\alpha_0$  and  $\alpha_q$  are the real-valued amplitudes of the elastically and inelastically scattered electric field components, respectively. Counter-intuitively, this implies that the measurement imprecision is independent of the overlap of  $\mathbf{E}^{(q)}(x, y)$  and the elastically scattered or LO fields, despite the interference of these fields being required to generate terms linearly proportional to the nanoparticle's motion in the recovered power (see Appendix C in the Supplementary material). More importantly, it implies that, due to the large values of  $\eta_q^{\ell,m}$  reported in Fig. 3, our technique should enable for higher measurement efficiencies than observed in conventional detection systems despite filtering out significant amounts of the incident light. This advantage is reflected in the signal-to-noise ratios observed in Fig. 2(b), which we note are unusually high for the transverse DOFs, with an optimal value of  $\text{SNR}_x^{\text{LP}_{11a}} \approx 110$  dB above the shot noise floor.

Finally, note that the LO field, as the dominant electric field component, usually also serves to offset the recovered signal, ensuring it sits above the system's technical noise [27]. Since the LO does not couple into the LP<sub>11a/b</sub> modes to provide this offset, the power in these channels is much weaker than in the LP<sub>01</sub> mode ( $< 10\%$ ). Consequently, if one were to measure every LP mode simultaneously with a single detector,  $S_{zz}(\Omega)$  would dominate the measurement result, and the transverse DOFs would be difficult to discern. This is why a spatial mode sorter must be used, as opposed to a simple few-mode fiber con-

figuration, and explains why the benefits of this approach have yet to be observed in previous experiments.

As a proof-of-principle demonstration of our detection technique, we use parametric feedback cooling to control the COM motion of a levitated nanoparticle. The temperature  $T_q$  achieved along the  $\hat{e}_q$  axis is determined by fitting the PSD measured at the appropriate output channel of the photonic chip (see Supplementary Material, Appendix H). To capture the actual dynamics of the system, the collected signals have been averaged over many periods of oscillation. Using this setup, we cool the motion of the nanoparticle from thermal equilibrium (300 K) to a minimum temperature of  $(T_x, T_y, T_z) = (7, 106, 21.4) \pm (3.1, 12, 2.3)$  mK, respectively. Interestingly, the minimum temperatures achieved here are an order of magnitude below what has been reported in the literature at pressures of approximately  $5 \times 10^{-5}$  mbar [21], the current technical limitation of our vacuum chamber. Indeed, we find that our observed values are approaching the theoretically predicted minimum values at this pressure (see Supplementary Material, Appendix I).

We note that  $T_x$  is the lowest observed temperature despite having the lowest measurement efficiency. We believe this is because  $\Omega_y \approx 2\Omega_z$ , such that the feedback signal generated for  $z(t)$  inadvertently drives the nanoparticle's motion along  $\hat{e}_y$ . This can be possibly avoided by varying the ellipticity of the polarisation of the trapping beam, which tunes the transverse oscillation frequencies [28]. However, this also leads to modifications in the spatial profile of the scattered field, to the detriment of the demultiplexing protocol (see Supplementary Material, Appendix J).

Information	Efficiencies	Values
Collection Efficiency		$\begin{cases} 0.50 & , x(t) \\ 0.50 & , y(t) \\ 0.90 & , z(t) \end{cases}$
Path Losses		0.90
Insertion Losses		0.79
Polarization-dependent Losses		0.99
Coupling Efficiency		$\begin{cases} 0.71 & , x(t) \rightarrow \text{LP}_{11a} \\ 0.81 & , y(t) \rightarrow \text{LP}_{11b} \\ 0.92 & , z(t) \rightarrow \text{LP}_{01} \end{cases}$
Quantum Efficiency		0.72
Dark Noise		0.79
Digital Noise		0.98
Measurement Efficiency ( $\eta_{tot}^{(q)}$ )		$\begin{cases} 0.14 & , x(t) \rightarrow \text{LP}_{11a} \\ 0.16 & , y(t) \rightarrow \text{LP}_{11b} \\ 0.32 & , z(t) \rightarrow \text{LP}_{01} \end{cases}$

TABLE I. Total efficiencies for the setup considered here. For a discussion on how each term has been determined, refer to the Supplementary Material, Appendix E.

In an effort to explain the improved performance of our parametric feedback cooling, we have opted to cal-

culate the measurement efficiencies of this setup for each translational DOF. To understand why this quantity is of interest, note that optical measurements necessarily disturb the system's natural evolution due to back-action. However, efficient measurements maximise the information gained per disturbance, and so can generate real-time feedback which not only controls the system's mechanical motion but also cancels the effects of said back-action.

We outline the information efficiencies of our system in Table I, where we report record measurement efficiencies for the transverse DOFs. Importantly, this is not at the expense of the longitudinal DOF, for which we achieve a value comparable to previous experimental demonstrations of 1D ground state cooling [2, 3]. From these values, we can estimate the minimum achievable phonon occupancy for the nanoparticle's COM motion along each spatial axis [3, 29, 30] in the limit of low pressures, where environmental information loss from random collisions with background gas molecules is negligible ( $\approx 1 \times 10^{-8}$  mbar) [31]. Under these conditions, with an optimised feedback circuit, we expect to reach phonon occupancies of  $\bar{n}_{\min}^q = (1 / \sqrt{\eta_{\text{tot}}^q} - 1) / 2$ . For the setup reported here, this is equivalent to  $(\bar{n}_{\min}^x, \bar{n}_{\min}^y, \bar{n}_{\min}^z) = (0.84, 0.75, 0.38)$  phonons. Hence, this is the first demonstration of a detection system capable of realizing the 3D motional quantum ground state of a levitated nanoparticle using measurement-based control techniques.

In summary, we have realized a novel approach to measuring the center-of-mass motion of a levitated dipolar scatterer, wherein the scattered field couples into an on-chip spatial mode sorter. By decomposing the inelastically scattered contributions to this field in the LP mode basis of an optical fiber, we can isolate contributions from each translational DOF in the amplitude of orthogonal optical modes. Thanks to this technique, we report record high, quantum-enabling measurement efficiencies for the translational degrees of freedom, which suggests that our technique can realize the 3D motional

quantum ground state. Importantly, we believe that our technique can be extended to higher-order modes in the LP basis and generalized to other families such as Hermite-Gaussian (HG) modes, orbital angular momentum (OAM) modes, and Laguerre-Gaussian (LG) modes. This opens an exciting avenue for tracking the entire 6D (rotational and translational) motion of levitated objects with arbitrarily high precision. Alternatively, one could harness the toolbox of structured light to match the inelastically scattered field of the levitated object perfectly. It is worth acknowledging that although the present demonstration focuses on the field of levitated optomechanics, the technique has the potential to be employed with other trapped microscopic objects such as trapped ions or neutral atoms where independently and directly accessing their different motional states, i.e. bosonic modes, could prove practical for hybrid qubit-oscillator quantum information processing [32–34].

Finally, the ability of the spatial mode sorter to isolate the scattered electric field associated with particular motional degrees of freedom is an essential step towards the passive, all-optical coherent feedback control of a levitated particle in free space. Close to the ground state, coherent feedback has the potential to improve cooling by avoiding measurement and feedback noise [19] and provides an avenue to generate mechanical squeezing [35].

## ACKNOWLEDGEMENT

Authors acknowledge fruitful discussions with Thiago Guerreiro, Michael Steel and Massimiliano Rossi. This work was supported by the Australian Research Council Centre of Excellence for Engineered Quantum Systems (Grant No. CE170100009) and Lockheed Martin. C. L. acknowledges support from the Sydney Quantum Academy Postdoctoral Research Fellowship. M. K. S. acknowledges support from the Australian Research Council Discovery Early Career Researcher Award (DE220101272).

- 
- [1] U. Delić, M. Reisenbauer, K. Dare, D. Grass, V. Vuletić, N. Kiesel, and M. Aspelmeyer, Cooling of a levitated nanoparticle to the motional quantum ground state, *Science* **367**, 892 (2020).
  - [2] L. Magrini, P. Rosenzweig, C. Bach, A. Deutschmann-Olek, S. G. Hofer, S. Hong, N. Kiesel, A. Kugi, and M. Aspelmeyer, Real-time optimal quantum control of mechanical motion at room temperature, *Nature* **595**, 373 (2021).
  - [3] F. Tebbenjohanns, M. L. Mattana, M. Rossi, M. Frimmer, and L. Novotny, Quantum control of a nanoparticle optically levitated in cryogenic free space, *Nature* **595**, 378 (2021).
  - [4] M. Kamba, R. Shimizu, and K. Aikawa, Optical cold damping of neutral nanoparticles near the ground state in an optical lattice, *Optics Express* **30**, 26716 (2022).
  - [5] D. C. Moore, A. D. Rider, and G. Gratta, Search for Millicharged Particles Using Optically Levitated Microspheres, *Physical Review Letters* **113**, 251801 (2014).
  - [6] S. Bose, A. Mazumdar, G. W. Morley, H. Ulbricht, M. Toroš, M. Paternostro, A. A. Geraci, P. F. Barker, M. Kim, and G. Milburn, Spin Entanglement Witness for Quantum Gravity, *Physical Review Letters* **119**, 240401 (2017).
  - [7] G. Afek, D. Carney, and D. C. Moore, Coherent Scattering of Low Mass Dark Matter from Optically Trapped Sensors, *Physical Review Letters* **128**, 101301 (2022).
  - [8] E. Kilian, M. Rademacher, J. M. H. Gosling, J. H. Iacoponi, F. Alder, M. Toroš, A. Pontin, C. Ghag, S. Bose, T. S. Monteiro, and P. F. Barker, Dark matter searches with levitated sensors, *AVS Quantum Science* **6**, 030503 (2024).

- [9] M. Scala, M. S. Kim, G. W. Morley, P. F. Barker, and S. Bose, Matter-Wave Interferometry of a Levitated Thermal Nano-Oscillator Induced and Probed by a Spin, *Physical Review Letters* **111**, 180403 (2013).
- [10] Y. Y. Fein, P. Geyer, P. Zwick, F. Kialka, S. Pedalino, M. Mayor, S. Gerlich, and M. Arndt, Quantum superposition of molecules beyond 25 kDa, *Nature Physics* **15**, 1242 (2019).
- [11] M. Arndt and K. Hornberger, Testing the limits of quantum mechanical superpositions, *Nature Physics* **10**, 271 (2014).
- [12] J. Piotrowski, D. Windey, J. Vijayan, C. Gonzalez-Ballester, A. de los Ríos Sommer, N. Meyer, R. Quidant, O. Romero-Isart, R. Reimann, and L. Novotny, Simultaneous ground-state cooling of two mechanical modes of a levitated nanoparticle, *Nature Physics* **19**, 1009 (2023).
- [13] A. Ranfagni, K. Børkje, F. Marino, and F. Marin, Two-dimensional quantum motion of a levitated nanosphere, *Physical Review Research* **4**, 033051 (2022).
- [14] F. Tebbenjohanns, M. Frimmer, and L. Novotny, Optimal position detection of a dipolar scatterer in a focused field, *Physical Review A* **100**, 043821 (2019).
- [15] P. Maurer, C. Gonzalez-Ballester, and O. Romero-Isart, Quantum theory of light interaction with a Lorenz-Mie particle: Optical detection and three-dimensional ground-state cooling, *Physical Review A* **108**, 033714 (2023).
- [16] L. Dania, K. Heidegger, D. S. Bykov, G. Cerchiari, G. Araneda, and T. E. Northup, Position Measurement of a Levitated Nanoparticle via Interference with Its Mirror Image, *Physical Review Letters* **129**, 013601 (2022).
- [17] S. Lloyd, Coherent quantum feedback, *Physical Review A* **62**, 022108 (2000).
- [18] J. Zhang, Y.-x. Liu, R.-B. Wu, K. Jacobs, and F. Nori, Quantum feedback: Theory, experiments, and applications, *Physics Reports* **679**, 1 (2017).
- [19] M. Ernzer, M. Bosch Aguilera, M. Brunelli, G.-L. Schmid, T. M. Karg, C. Bruder, P. P. Potts, and P. Treutlein, Optical Coherent Feedback Control of a Mechanical Oscillator, *Physical Review X* **13**, 021023 (2023).
- [20] J. Gieseler, B. Deutsch, R. Quidant, and L. Novotny, Subkelvin parametric feedback cooling of a laser-trapped nanoparticle, *Physical Review Letters* **109**, 10.1103/PhysRevLett.109.103603 (2012).
- [21] J. Vovrosh, M. Rashid, D. Hempston, J. Bateman, M. Paternostro, and H. Ulbricht, Parametric feedback cooling of levitated optomechanics in a parabolic mirror trap, *JOSA B* **34**, 1421 (2017).
- [22] LPMUX Series Multiplexer (2019).
- [23] N. Riesen and J. D. Love, Ultra-Broadband Tapered Mode-Selective Couplers for Few-Mode Optical Fiber Networks, *IEEE Photonics Technology Letters* **25**, 2501 (2013).
- [24] S. Gross, N. Riesen, J. D. Love, and M. J. Withford, Three-dimensional ultra-broadband integrated tapered mode multiplexers, *Laser & Photonics Reviews* **8**, L81 (2014).
- [25] J. Gieseler, M. Spasenović, L. Novotny, and R. Quidant, Nonlinear Mode Coupling and Synchronization of a Vacuum-Trapped Nanoparticle, *Physical Review Letters* **112**, 103603 (2014).
- [26] A. T. M. A. Rahman, A. C. Frangeskou, P. F. Barker, and G. W. Morley, An analytical model for the detection of levitated nanoparticles in optomechanics, *Review of Scientific Instruments* **89**, 023109 (2018).
- [27] L. S. Madsen, M. Waleed, C. A. Casacio, A. Terrasson, A. B. Stilgoe, M. A. Taylor, and W. P. Bowen, Ultrafast viscosity measurement with ballistic optical tweezers, *Nature Photonics* **15**, 386 (2021).
- [28] C. Laplane, P. Ren, R. P. Roberts, Y. Lu, and T. Volz, Inert shell coating for enhanced laser refrigeration of nanoparticles: application in levitated optomechanics (2023).
- [29] H. M. Wiseman and G. J. Milburn, *Quantum Measurement and Control* (Cambridge University Press, 2009).
- [30] M. Rossi, D. Mason, J. Chen, Y. Tsaturyan, and A. Schliesser, Measurement-based quantum control of mechanical motion, *Nature* **563**, 53 (2018).
- [31] A. A. Clerk, M. H. Devoret, S. M. Girvin, F. Marquardt, and R. J. Schoelkopf, Introduction to quantum noise, measurement, and amplification, *Reviews of Modern Physics* **82**, 1155 (2010).
- [32] C. Flühmann, T. L. Nguyen, M. Marinelli, V. Negnevitsky, K. Mehta, and J. P. Home, Encoding a qubit in a trapped-ion mechanical oscillator, *Nature* **566**, 513 (2019).
- [33] T. Navickas, R. J. MacDonell, C. H. Valahu, V. C. Olaya-Agudelo, F. Scuccimarra, M. J. Millican, V. G. Matsos, H. L. Nourse, A. D. Rao, M. J. Biercuk, C. Hempel, I. Kassal, and T. R. Tan, Experimental Quantum Simulation of Chemical Dynamics (2024).
- [34] Y. Liu, S. Singh, K. C. Smith, E. Crane, J. M. Martyn, A. Eickbusch, A. Schuckert, R. D. Li, J. Sinanan-Singh, M. B. Soley, T. Tsunoda, I. L. Chuang, N. Wiebe, and S. M. Girvin, Hybrid Oscillator-Qubit Quantum Processors: Instruction Set Architectures, Abstract Machine Models, and Applications (2024).
- [35] T. M. Karg, B. Gouraud, P. Treutlein, and K. Hammerer, Remote Hamiltonian interactions mediated by light, *Physical Review A* **99**, 063829 (2019).
- [36] M. A. Lieb and A. J. Meixner, A high numerical aperture parabolic mirror as imaging device for confocal microscopy, *Optics Express* **8**, 458 (2001).
- [37] R. E. Wagner and W. J. Tomlinson, Coupling efficiency of optics in single-mode fiber components, *Applied Optics* **21**, 2671 (1982).

## Supplementary Material: Three-dimensional quantum-enabling displacement sensing of a levitated nanoparticle

### Appendix A: Decomposition of the scattered field

In this Appendix we provide the explicit expressions for the field scattered from a levitated dipolar scatterer, having been transformed by the parabolic mirror and collection lens composing the optical trap. In the Fraunhofer approximation, the scattered field is analogous to the far-field of an electric dipole, with an appropriate phase-shift:

$$\mathbf{E}_{\text{scat}}(\omega, \mathbf{r}; \mathbf{q}(t)) \approx \mathbf{E}_{\text{dip}}(\omega, \mathbf{r}) \exp \left[ -ik \left( \frac{\mathbf{r} \cdot \mathbf{q}(t)}{|\mathbf{r}|} \right) \right], \quad (\text{A1})$$

where

$$\mathbf{E}_{\text{dip}}(\omega, \mathbf{r}) = \frac{k^2}{4\pi\epsilon_0} \frac{e^{ik|\mathbf{r}|}}{|\mathbf{r}|} [\mathbf{r} \times \mathbf{p}(\omega, \mathbf{r})] \times \mathbf{r}. \quad (\text{A2})$$

Here,  $\mathbf{q}(t)$  refers to the nanoparticle's real-time displacement from the focal point of the parabolic mirror, and  $\mathbf{p}(\omega, \mathbf{r})$  to the induced dipole moment, which we assume is aligned parallel to the polarization axis of the trapping beam. Moving forward, we drop the frequency dependence of these terms, and choose to focus on the case of a monochromatic trapping beam. We note that Eq. (A1) does not describe the electric field observed at the input to the space-division demultiplexing photonic chip, however. Instead, the scattered field is transformed by a series of optical elements, resulting in modifications to both the spatially-varying phase and amplitude. In particular, for the optical trap design considered here, the back-scattered component of the field is first collimated by a gold-coated, high-numerical aperture (NA) parabolic mirror. We write the effective NA of this device as being of the form

$$\text{NA} = 1 - \cos \left( \arctan \left[ \frac{r_m}{f_m - \frac{r_m^2}{4f_m}} \right] \right), \quad (\text{A3})$$

where  $f_m$  and  $r_m$  are the focal length (1 mm) and radius (2 mm) of the parabolic mirror, respectively [21]. The collimated field then propagates to some collection lens of focal length  $f_{cl}$  (25 mm) and is subsequently focused in the input plane of the photonic chip. A schematic of this setup is shown in Fig. 4 below.

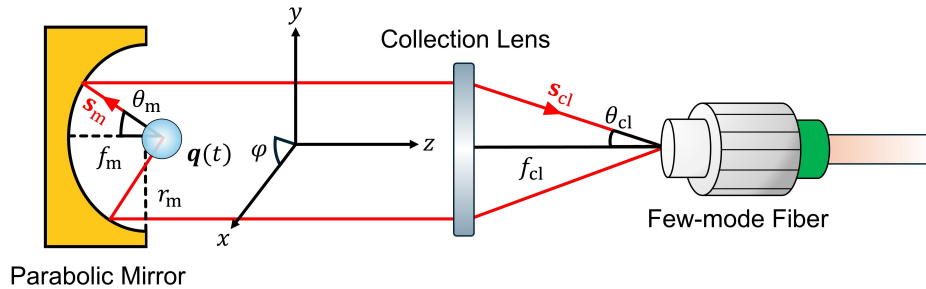


FIG. 4. Geometry of the parabolic mirror being modelled, with key features labelled. A nanoparticle trapped at the diffraction-limited focal point of the parabolic mirror scatters a portion of the incident light, which is then coupled into the few-mode fiber input of a space-division demultiplexing photonic chip.

This problem, of imaging the light scattered from a dipolar source, has been studied extensively in the context of confocal microscopy [36], where it is typically addressed using angular spectrum theory. For the setup considered here, we find a time-independent component of the electric field, in the focal plane of the collection lens, of the form

$$\begin{aligned} \mathbf{E}_{\text{scat}}(x, y; \mathbf{q}(t)) = & -\frac{ik^3 f_{cl}}{16\pi^3 \epsilon_0} \int_0^{\theta_{cl}^{\text{max}}} \int_0^{2\pi} \frac{[1 + \cos(\theta_m)]}{2f_m} \sqrt{\cos(\theta_{cl})} \left[ (\mathbf{p} \cdot \mathbf{e}_m^{\parallel}) \cdot \mathbf{e}_{cl}^{\parallel} - (\mathbf{p} \cdot \mathbf{e}_{\perp}) \cdot \mathbf{e}_{\perp} \right] \\ & \times \exp \left[ -ik(x \sin(\theta_{cl}) \cos(\varphi) + y \sin(\theta_{cl}) \sin(\varphi) + (\hat{\mathbf{e}}_q \cdot \mathbf{s}_m) q(t)) \right] \sin(\theta_{cl}) \, d\theta_{cl} d\varphi, \end{aligned} \quad (\text{A4})$$

where we have introduced the relevant unit vectors,

$$\mathbf{e}_\perp = \left[ -\sin(\varphi), \cos(\varphi), 0 \right] \quad (\text{A5})$$

$$\mathbf{e}_m^\parallel = \left[ \cos(\theta_m)\cos(\varphi), \cos(\theta_m)\sin(\varphi), \sin(\theta_m) \right] \quad (\text{A6})$$

$$\mathbf{e}_{cl}^\parallel = \left[ -\cos(\theta_{cl})\cos(\varphi), -\cos(\theta_{cl})\sin(\varphi), -\sin(\theta_{cl}) \right] \quad (\text{A7})$$

$$\mathbf{s}_m = \left[ \sin(\theta_m)\cos(\varphi), \sin(\theta_m)\sin(\varphi), -\cos(\theta_m) \right]. \quad (\text{A8})$$

Here,  $2 / [1 + \cos(\theta_m)]$  and  $\sqrt{\cos(\theta_{cl})}$  are the apodization factors of the parabolic mirror and collections lens, respectively. Defining the magnification factor as  $M = f_{cl} / f_m$ , we have

$$\theta_m = 2 \arctan \left( \frac{M \sin(\theta_{cl})}{2} \right) \quad (\text{A9})$$

$$\theta_{cl}^{\max} = \arctan \left( \frac{2r_m}{f_{cl}} \right), \quad (\text{A10})$$

where  $M = 25$  and  $\theta_{cl}^{\max} \approx 0.16$  radians for the particular experimental setup considered here. Taylor expanding the exponential term in Eq. (A4) to first-order about  $\mathbf{q} = \mathbf{0}$ , we find that we can write the scattered field as

$$\mathbf{E}_{\text{scat}}(x, y; \mathbf{q}(t)) = \mathbf{E}_{\text{scat}}(x, y; \mathbf{q} = \mathbf{0}) + \overset{\leftrightarrow}{\mathbf{J}}_{\text{scat}}(x, y; \mathbf{q} = \mathbf{0})\mathbf{q}(t)^T, \quad (\text{A11})$$

where we have introduced the Jacobian tensor

$$\overset{\leftrightarrow}{\mathbf{J}}_{\text{scat}}(x, y; \mathbf{q} = \mathbf{0}) = \begin{bmatrix} \nabla^T \mathbf{E}_{\text{scat}}(x, y; \mathbf{q} = \mathbf{0}) \cdot \hat{\mathbf{e}}_x \\ \nabla^T \mathbf{E}_{\text{scat}}(x, y; \mathbf{q} = \mathbf{0}) \cdot \hat{\mathbf{e}}_y \\ \nabla^T \mathbf{E}_{\text{scat}}(x, y; \mathbf{q} = \mathbf{0}) \cdot \hat{\mathbf{e}}_z \end{bmatrix}, \quad (\text{A12})$$

for

$$\nabla^T f = \left[ \frac{\partial f}{\partial(\mathbf{q} \cdot \hat{\mathbf{e}}_x)}, \frac{\partial f}{\partial(\mathbf{q} \cdot \hat{\mathbf{e}}_y)}, \frac{\partial f}{\partial(\mathbf{q} \cdot \hat{\mathbf{e}}_z)} \right]. \quad (\text{A13})$$

For the simplest case where the nanoparticle oscillates about a single spatial axis, such that  $\mathbf{q}(t) = q(t)\hat{\mathbf{e}}_q$  for some principle axis  $q = x, y$  or  $z$ , Eq. (A11) reduces to

$$\begin{aligned} \mathbf{E}_{\text{scat}}(x, y; \mathbf{q}(t)) &= \mathbf{E}_{\text{scat}}(x, y; \mathbf{q} = \mathbf{0}) + q(t) \frac{\partial \mathbf{E}_{\text{scat}}(x, y; \mathbf{q} = \mathbf{0})}{\partial(\mathbf{q} \cdot \hat{\mathbf{e}}_q)} \\ &= \mathbf{E}_0(x, y) + \frac{q(t)}{w_0} \mathbf{E}^{(q)}(x, y), \end{aligned} \quad (\text{A14})$$

where  $w_0$  refers to the beam waist at the focal point of the parabolic mirror, and has been introduced to normalize  $q(t)$ . Upon inspection, we find that this is equivalent to decomposing the total field into elastically and inelastically scattered contributions.

## Appendix B: Calculating the coupling efficiencies

To calculate the coupling of each scattered field component into the space-division demultiplexing photonic chip (spatial mode sorter), we need to formulate the guided modes. The input to the chip is an embedded few-mode, graded-index optical fiber (FMF) designed for operation at  $\lambda = 1550$  nm, with a core radius ( $r_{\text{fib}}$ ) of approximately 4  $\mu\text{m}$ . Due to the low refractive index contrast between the refractive indices of the core ( $n_1$ ) and cladding ( $n_2$ ) we treat the guided modes as linearly-polarized (LP) modes, whose electric field distributions are fully described by the family of complex amplitude functions

$$\text{LP}_{\ell, m}(\mathbf{r}) = \begin{cases} J_\ell \left( \frac{u\sqrt{x^2+y^2}}{r_{\text{fib}}} \right) \cos(\ell\phi) \exp[-i\beta_{\ell, m}z] & , \sqrt{x^2+y^2} \leq r_{\text{fib}} \\ \frac{J_\ell(u)}{K_\ell(w)} K_\ell \left( \frac{w\sqrt{x^2+y^2}}{r_{\text{fib}}} \right) \cos(\ell\phi) \exp[-i\beta_{\ell, m}z] & , \sqrt{x^2+y^2} \geq r_{\text{fib}} \end{cases} \quad (\text{B1})$$



where we have defined the quantities

$$u = r_{\text{fib}} \sqrt{n_1^2 k^2 - \beta_{\ell,m}^2} \quad (\text{B2})$$

$$w = r_{\text{fib}} \sqrt{\beta_{\ell,m}^2 - n_2^2 k^2}, \quad (\text{B3})$$

in terms of the *propagation constant*,  $\beta_{\ell,m}$ . Here,  $J_\ell(\bullet)$  and  $K_\ell(\bullet)$  refer to Bessel functions of the first kind, and modified Bessel functions of the second kind, respectively. In our particular setup, the spatial profile of each LP mode is rotated anti-clockwise through an angle of approximately  $\theta = 14^\circ$  from the laboratory frame of reference. To account for this, we transform the vector field of each LP mode according to

$$\mathbf{LP}_{\ell,m}(\mathbf{r}) = R(\theta) \mathbf{LP}_{\ell,m}(\mathbf{r}') \hat{e}_x, \quad (\text{B4})$$

where  $\mathbf{r}' = R^T(\theta) \mathbf{r}$  and we have assumed that we are concerned with only those LP modes polarised along the  $\hat{e}_x$  axis. To perform this calculation, we have made use of the usual rotation matrix

$$R(\theta) = \begin{bmatrix} \cos(\theta) & \sin(\theta) & 0 \\ -\sin(\theta) & \cos(\theta) & 0 \\ 0 & 0 & 1 \end{bmatrix}. \quad (\text{B5})$$

Additionally, to accommodate for the angled end-face of the FMF, the photonic chip is inclined by approximately  $\phi = 5^\circ$  to the propagation axis. This introduces a weak longitudinally-polarised component to each LP mode. Hence, repeating the calculations above for a secondary rotation matrix

$$R(\phi) = \begin{bmatrix} 1 & 0 & 0 \\ 0 & \cos(\phi) & \sin(\phi) \\ 0 & -\sin(\phi) & \cos(\phi) \end{bmatrix}, \quad (\text{B6})$$

we may define a set of electric fields

$$\mathbf{LP}_{\ell,m}(\mathbf{r}) = \mathbf{LP}_{\ell,m}(\mathbf{r}'') \begin{bmatrix} \cos(\theta) \\ -\sin(\theta)\cos(\phi) \\ \sin(\theta)\sin(\phi) \end{bmatrix}, \quad (\text{B7})$$

in terms of the modified coordinates

$$\mathbf{r}'' = \begin{bmatrix} x \cos(\theta) - y \sin(\theta) \\ \cos(\phi)[x \sin(\theta) + y \cos(\theta)] - z \sin(\phi) \\ \sin(\phi)[x \sin(\theta) + y \cos(\theta)] + z \cos(\phi) \end{bmatrix}. \quad (\text{B8})$$

Importantly, these fields remain mutually orthogonal with respect to the normalized inner-product

$$\left| \iint_{-\infty}^{\infty} \mathbf{LP}_{\ell_1,m_1}^*(x,y) \cdot \mathbf{LP}_{\ell_2,m_2}(x,y) \, dx dy \right| = 0, \quad (\text{B9})$$

for all  $(\ell_1, m_1) \neq (\ell_2, m_2)$ . To calculate the coupling of the inelastically scattered field  $\mathbf{E}^{(q)}(x,y)$  into any given LP mode, we calculate the quantity

$$\eta_q^{\ell,m} = \frac{\left| \iint_{\text{FMF}} [\mathbf{E}^{(q)}(x,y)]^* \cdot \mathbf{LP}_{\ell,m}(x,y) \, dx dy \right|}{\sqrt{\iint_{\text{FMF}} |\mathbf{E}^{(q)}(x,y)|^2 \, dx dy \times \iint_{\text{FMF}} |\mathbf{LP}_{\ell,m}(x,y)|^2 \, dx dy}}, \quad (\text{B10})$$

where integration is carried out over the input face of the few-mode input fiber (FMF). Finally, we note that Eq. (B10) is an approximate expression for the coupling coefficient, derived under the assumption that the coupled modes are exclusively transverse and spatially polarisation-matched [37], and that reflection from the face of the FMF is negligible. In this demonstration both conditions are approximately fulfilled, owing to the natural transverse characteristics of the LP modes, and the small contrast between air and fiber material ( $n = 1.4679$ ). Exact analysis of the coupling, employing numerical modelling of the coupling between the scattered fields and an optimised set of fiber modes, will be published elsewhere.

### Appendix C: Deriving the measurement imprecision

We must realistically consider the coupling of the total scattered field into the spatial mode sorter, not just the inelastically scattered term  $\mathbf{E}^{(q)}(x, y)$ . First, however, let us consider the form of the total electric field incident on the input plane of the spatial mode sorter. For the case where the nanoparticle oscillates only along the  $\hat{\mathbf{e}}_q$  axis, this field is of the form

$$\mathbf{E}_{\text{inc}}(x, y) = \mathbf{E}_{\text{ref}}(x, y) + \mathbf{E}_0(x, y) + \frac{q(t)}{w_0} \mathbf{E}^{(q)}(x, y). \quad (\text{C1})$$

Moving forward, we choose to represent the electric field in terms of the complex normalised modes  $\hat{\mathbf{E}}(x, y) = \mathbf{E}(x, y) / (\iint_{\text{FMF}} |\mathbf{E}(x, y)|^2 dx dy)^{1/2}$  and corresponding real-valued amplitudes  $\alpha$ . To this end, we write

$$\mathbf{E}_{\text{inc}}(x, y) = \hat{\mathbf{E}}_{\text{ref}}(x, y) \alpha_{\text{ref}} + \hat{\mathbf{E}}_0(x, y) \alpha_0 + \frac{q(t)}{w_0} \hat{\mathbf{E}}^{(q)}(x, y) \alpha_q. \quad (\text{C2})$$

The electric field excited in the  $\text{LP}_{\ell, m}$  channel of the spatial mode sorter is then

$$\mathbf{LP}_{\ell, m}(x, y) = \hat{\mathbf{LP}}_{\ell, m}(x, y) \left[ \eta_{\text{ref}}^{\ell, m} \alpha_{\text{ref}} + \eta_0^{\ell, m} \alpha_0 + \frac{q(t)}{w_0} \eta_q^{\ell, m} \alpha_q \right], \quad (\text{C3})$$

where  $\eta_{\text{ref}}^{\ell, m}$  and  $\eta_0^{\ell, m}$  are defined analogously to Eq. (B10) except for the LO and elastically scattered fields, respectively. Neglecting any internal losses, we expect that the output power in the  $\text{LP}_{\ell, m}$  channel measured by the detector can therefore be estimated as

$$\begin{aligned} P_q^{\ell, m}(t) &= \sqrt{\frac{\varepsilon_0}{\mu_0}} \left| \eta_0^{\ell, m} \alpha_0 + \frac{q(t)}{w_0} \eta_q^{\ell, m} \alpha_q + \eta_{\text{ref}}^{\ell, m} \alpha_{\text{ref}} \right|^2 \\ &= \sqrt{\frac{\varepsilon_0}{\mu_0}} \left( (\eta_{\text{ref}}^{\ell, m})^2 \alpha_{\text{ref}}^2 + (\eta_0^{\ell, m})^2 \alpha_0^2 + 2\eta_{\text{ref}}^{\ell, m} \eta_0^{\ell, m} \alpha_{\text{ref}} \alpha_0 + 2\frac{q(t)}{w_0} \eta_{\text{ref}}^{\ell, m} \eta_q^{\ell, m} \alpha_{\text{ref}} \alpha_q + 2\frac{q(t)}{w_0} \eta_0^{\ell, m} \eta_q^{\ell, m} \alpha_0 \alpha_q \right), \end{aligned} \quad (\text{C4})$$

where we have discarded the term proportional to  $[q(t) / w_0]^2$  as we expect the displacements to be far smaller than  $w_0$  along each axis. Note that, from Eq. (C4), we do not simply measure  $q(t)$ . Instead, the measurement result is dominated by a series of time-independent coefficients, which mask the information available on the nanoparticle's position. From the form of these coefficients, we can estimate the measurement imprecision. This involves first collecting those terms independent of the nanoparticle's motion, which we identify as contributing only shot noise, and so have a power spectral density (PSD) of the form

$$S_{\text{noise}}^{\ell, m} = \frac{\hbar k c}{2\pi} \sqrt{\frac{\varepsilon_0}{\mu_0}} \left( (\eta_{\text{ref}}^{\ell, m})^2 \alpha_{\text{ref}}^2 + (\eta_0^{\ell, m})^2 \alpha_0^2 + 2\eta_{\text{ref}}^{\ell, m} \eta_0^{\ell, m} \alpha_{\text{ref}} \alpha_0 \right). \quad (\text{C5})$$

Additionally,  $q(t)$  is weighted by a factor of

$$\beta_q^{\ell, m} = \frac{2}{w_0} \sqrt{\frac{\varepsilon_0}{\mu_0}} \left( \eta_{\text{ref}}^{\ell, m} \eta_q^{\ell, m} \alpha_{\text{ref}} \alpha_q + \eta_0^{\ell, m} \eta_q^{\ell, m} \alpha_0 \alpha_q \right), \quad (\text{C6})$$

which is squared when calculating the PSD. The imprecision associated with measuring the nanoparticle's motion along the  $\hat{\mathbf{e}}_q$  axis, in the  $\text{LP}_{\ell, m}$  output channel of the spatial mode sorter, will therefore be of the form  $S_{\text{imp}, q}^{\ell, m} = S_{\text{noise}}^{\ell, m} / (\beta_q^{\ell, m})^2$  [14, 15]. Let us now consider how one might go about minimising this measurement imprecision. In particular, given the coupling coefficients calculated in Fig. 3 of the main text, we opt to consider the case wherein the LO field is effectively decoupled from each LP mode ( $\eta_{\text{ref}}^{\ell, m} = 0$ ). In this case, the measurement imprecision reduces to

$$S_{\text{imp}, q}^{\ell, m} = \frac{\hbar k c}{8\pi} \sqrt{\frac{\mu_0}{\varepsilon_0}} \frac{1}{\alpha_q^2} \frac{w_0^2}{(\eta_q^{\ell, m})^2}, \quad (\text{C7})$$

which is minimised when  $\eta_q^{\ell, m} = 1$ . Perhaps counter-intuitively, this result suggests that the measurement imprecision is independent of the overlap of the inelastically and elastically scattered field, despite Eq. (C4) suggesting that our

measurement relies on the interference of these two fields. Note that, in the case where each LP mode is instead decoupled from the elastically scattered field ( $\eta_0^{\ell,m} = 0$ ), we arrive at a very similar result. That is,

$$S_{\text{imp},q}^{\ell,m} = \frac{\hbar kc}{8\pi} \sqrt{\frac{\mu_0}{\varepsilon_0}} \frac{1}{\alpha_q^2} \frac{w_0^2}{(\eta_q^{\ell,m})^2}, \quad (\text{C8})$$

which is independent of the overlap of the inelastically scattered and LO fields.

#### Appendix D: Form of the power spectral density

Let us now consider the form of the power spectral density (PSD) measured at each LP $_{\ell,m}$  output channel of the space-division de-multiplexing photonic chip. In Appendix C we argued that the power measured at a detector is given by Eq. (C4), and can be split into those terms independent of the nanoparticle's motion, and those terms proportional to  $q(t)$ . We have already identified the former as sources of noise in the measurement result, with a PSD given by Eq. (C5). Collecting the remaining terms, we introduce  $s_{qq}^{\ell,m}(t) = q(t)\beta_q^{\ell,m}$ , where  $\beta_q^{\ell,m}$  is defined in Eq. (C6). From the Wiener-Khinchin theorem, this quantity has a PSD of the form

$$\begin{aligned} S_{qq}^{\ell,m}(\Omega) &= \int_{-\infty}^{\infty} \langle s_{qq}^{\ell,m}(t)s_{qq}^{\ell,m}(t+\tau) \rangle e^{-i\Omega\tau} d\tau \\ &= (\beta_q^{\ell,m})^2 \int_{-\infty}^{\infty} \langle q(t)q(t+\tau) \rangle e^{-i\Omega\tau} d\tau. \end{aligned} \quad (\text{D1})$$

From the equation of motion for an optically-levitated nanoparticle, discussed in Appendix (G), the second term in this expression reduces to the well-known result

$$S_{qq}^{\ell,m}(\Omega) = (\beta_q^{\ell,m})^2 \frac{k_B T_0}{\pi m} \frac{\gamma}{(\Omega^2 - \Omega_0^2)^2 + \Omega^2 \gamma^2}. \quad (\text{D2})$$

The total PSD measured at each LP output channel of the space-division de-multiplexing photonic chip is then of the form

$$S_{\text{tot}}^{\ell,m}(\Omega) = S_{\text{imp},q}^{\ell,m} + S_{qq}^{\ell,m}(\Omega). \quad (\text{D3})$$

Here we see the role of the imprecision in this measurement, derived in Appendix (C), which functions as the noise floor of the PSD.

#### Appendix E: Discussion of losses and efficiencies

Here, we provide a brief overview of the efficiencies reported in the main text.

##### 1. Collection efficiency

We write the effective numerical aperture (NA) of the parabolic mirror as

$$\text{NA} = 1 - \cos \left( \arctan \left[ \frac{r_m}{f_m - \frac{r_m^2}{4f_m}} \right] \right), \quad (\text{E1})$$

where  $f_m$  and  $r_m$  are the focal length (1 mm) and radius (2 mm) of the parabolic mirror, respectively. For the design specifications used here, this implies a numerical aperture of  $\text{NA} = 1$ . Hence, we expect to collect all of the light back-scattered from an optically-levitated nanoparticle, equivalent to a photon collection efficiency of 50% for all three center-of-mass (COM) translational degrees of freedom (DOFs). In the context of information losses, however, we require a more nuanced approach. This is because motional information is not uniformly distributed in

the scattered field. To this end, we consider the so-called *information radiation patterns* (IRPs) associated with each COM translational DOF,  $q(t)$  for  $q = x, y, z$  [14, 15]. These IRPs are of the form

$$\mathcal{I}_x(\theta, \varphi) = \frac{15}{8\pi} \left[ 1 - \sin^2(\theta)\cos^2(\phi) \right] \sin^2(\theta)\cos^2(\varphi) \, d\Omega \quad (\text{E2})$$

$$\mathcal{I}_y(\theta, \varphi) = \frac{15}{16\pi} \left[ 1 - \sin^2(\theta)\cos^2(\phi) \right] \sin^2(\theta)\sin^2(\varphi) \, d\Omega \quad (\text{E3})$$

$$\mathcal{I}_z(\theta, \varphi) = \frac{3}{8\pi(\frac{2}{5} + A^2)} \left[ 1 - \sin^2(\theta)\cos^2(\phi) \right] (\cos(\theta) - A)^2 \, d\Omega, \quad (\text{E4})$$

for an  $x$ -polarised dipolar scatterer. Here,  $A$  is a consequence of the Gouy phase inherited from the trapping beam. Note that, for intermediate values of the numerical aperture, we find  $A \approx 1 - (kz_R)^{-1}$  for Rayleigh length  $z_R$ . Given that our setup operates well beyond this limit, however, we choose to focus on illumination by a plane wave ( $A = 1$ ). To determine the information collection efficiency for the parabolic mirror, we evaluate the integral

$$\eta_q = \int_0^{2\pi} \int_{\pi/2}^{\pi} \mathcal{I}_q(\theta, \varphi) \, d\theta d\varphi, \quad (\text{E5})$$

where the lower integration limit on  $\theta$  is given by  $\pi - \arcsin(\text{NA})$ . This represents the amount of information content collected in the back focal plane of the optical trap, and gives  $(\eta_x, \eta_y, \eta_z) = (50, 50, 90)\%$ , respectively.

## 2. Path losses

To estimate the path losses, we measure the difference in power of the forward- and backward-propagating trapping beam in the focal plane of the collection lens, with no nanoparticle trapped. From this, we arrive at a value for the path losses of approximately 10%, equivalent to an efficiency of 90%.

## 3. Coupling efficiency

Inspired by the ability of our numerical model to predict the selectivity of the spatial mode sorter, we use those coupling efficiencies reported in the main text.

## 4. Quantum efficiency

From the technical specifications provided by the supplier of the detectors used here (*PD100-DC*, *Koheron*), we estimate the quantum efficiency of our detectors to be 0.72% at  $\lambda = 1550$  nm.

## 5. Dark noise

Information loss must also be considered in the electronic line, after each signal has been measured. In particular, we note that the dark current noise will mask some of the available information. At frequencies near to the natural oscillation frequencies of the nanoparticle, we measure the dark noise to be approximately 8 dB below the shot noise, equivalent to an efficiency of 79%.

## 6. Digital noise

In the context of measurement-based control techniques, it is meaningful to consider those additional losses which stem from use of a digital feedback loop. In particular, here we are interested in using a Field Programmable Gate Array (FPGA) board (*STEMlab 125-14*, *Red Pitaya*) which functions as a phase-locked loop (PLL), with an estimated efficiency of 95%.

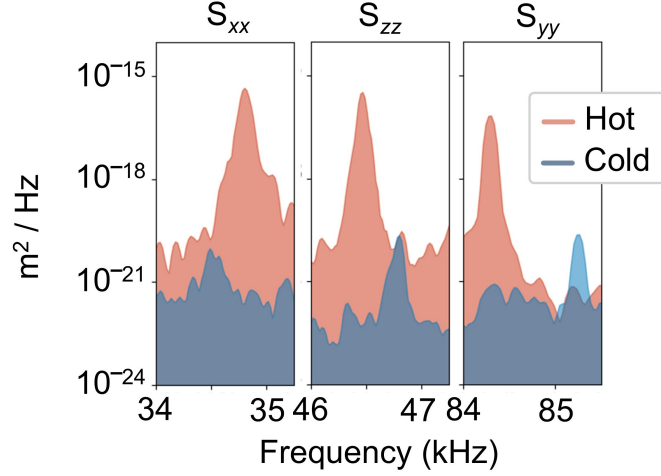


FIG. 5. Calibrated power spectral density (PSD)  $S_{qq}$  of the nanoparticle's COM motion at thermal equilibrium (300 K) and after having been cooled to a temperature of  $(T_x, T_y, T_z) = (7, 106, 21.4) \pm (3.1, 12, 2.3)$  mK at  $4.7 \times 10^{-5}$  mbar via parametric feedback cooling.

#### Appendix F: Feedback cooling data

Here we show a comparison of the power spectral densities (PSDs) for the nanoparticle's center-of-mass translational degrees of freedom at thermal equilibrium (300 K) ("Hot") and after having been cooled to a temperature of  $(T_x, T_y, T_z) = (7, 106, 21.4) \pm (3.1, 12, 2.3)$  mK ("Cold"). These results were measured at a pressure of  $4.7 \times 10^{-5}$  mbar, which is the current technical limitation of our vacuum chamber. To calibrate each PSD and estimate the corresponding temperatures we used those methods described in Appendices G and H, respectively.

#### Appendix G: Calculation of calibration factor

In the limit of small mechanical displacements, the thermally driven center-of-mass (COM) motion of an optically levitated dielectric nanoparticle can be approximated as simple harmonic motion. Specifically, we are interested in the limit where each of the three spatial dimensions are decoupled from one another, and so may be treated separately. Hence, in the presence of a feedback force, we write

$$\ddot{q}(t) + [\gamma + \delta\gamma_q] \dot{q}(t) + [\Omega_q + \delta\Omega_q]^2 q(t) = \frac{1}{m} \mathbf{F}_{\text{th}}^{(q)}(t), \quad (\text{G1})$$

where  $\gamma$  is the pressure-dependent damping rate of the nanoparticle's motion,  $\Omega_q$  is the characteristic frequency along the  $q$ -axis, and  $m$  is the nanoparticle's mass. Here,  $\mathbf{F}_{\text{th}}(t)$  is the Langevin force arising from the system's interaction with thermal background gas. In accordance with the fluctuation-dissipation theorem, this term satisfies

$$\langle \mathbf{F}_{\text{th}}(t) \mathbf{F}_{\text{th}}(t + \tau) \rangle = 2m\gamma k_B T_0 \delta(t - \tau). \quad (\text{G2})$$

Note that, in Eq. (G1) the feedback force is encoded in the linear shifts  $\delta\gamma_q$  and  $\delta\Omega_q$ , respectively. From this equation of motion, we can construct a power spectral density (PSD) for this system of the form

$$S_{(qq)}(\Omega) = \chi^2 \frac{k_B T_0}{\pi m} \frac{\gamma}{([\Omega_q + \delta\Omega_q]^2 - \Omega^2)^2 + \Omega^2 (\gamma + \delta\gamma_q)^2}, \quad (\text{G3})$$

where  $\chi$  is referred to as the *calibration factor*, in units of V / m. This term stems from the fact that most experimental PSDs, calculated from the time-trace recorded on a photodetector, are inherently in units of  $\text{V}^2 / \text{Hz}$ . However, given we are concerned with the motion of a nanoparticle, we require a PSD in units of  $\text{m}^2 / \text{Hz}$  to determine relevant quantities, such as the position resolution. Formally,  $\chi$  is equivalent to  $\beta_q^{\ell, m}$  from Appendices C and D multiplied by the responsivity (in units of V / W) of the detectors used. For ease of fitting, here we choose to simplify this PSD to one of the form

$$S_{qq}(\Omega) = \frac{A}{(B^2 - \Omega^2)^2 + \Omega^2 C^2}. \quad (\text{G4})$$

Hence, by fitting Eq. (G4) to data taken at thermal equilibrium ( $T_0 = 300$  K), we can extract the calibration factor in terms of known quantities. That is,

$$\chi = \sqrt{\frac{A}{C} \frac{\pi m}{k_B T_0}}. \quad (\text{G5})$$

### Appendix H: Temperature estimation

In Appendix G we claimed that an optically-levitated nanoparticle has a motional power spectral density (PSD) given by Eq. (G3). From the reciprocity of the Wiener-Khinchin theorem, this implies a mean-square displacement along the  $q$ -axis of the form

$$\langle q(t)q(t) \rangle = \frac{k_B T_0}{m (\Omega_q + \delta\Omega_q)^2} \frac{\gamma}{\gamma + \delta\gamma_q}. \quad (\text{H1})$$

According to the equipartition theorem of statistical mechanics, this quantity is related to the center-of-mass (COM) temperature  $T_q$  of the nanoparticle, such that

$$T_q = T_0 \frac{\gamma}{\gamma + \delta\gamma_q}. \quad (\text{H2})$$

Here, we use this relationship to estimate the temperature along each spatial axis after a nanoparticle has undergone parametric feedback cooling. To understand this process, consider fitting Eq. (G4) to experimental data of  $S_{qq}(\Omega)$  taken at thermal equilibrium ( $T_0 = 300$  K). From this, one recovers fit parameters  $A_0$ ,  $B_0$  and  $C_0$ , respectively. Conversely, for data taken of a cooled nanoparticle, we find fit parameters  $A_{\text{fb}}$ ,  $B_{\text{fb}}$  and  $C_{\text{fb}}$ . Hence, we calculate a COM temperature for the cooled nanoparticle,

$$T_q = T_0 \frac{A_{\text{fb}} C_0}{C_{\text{fb}} A_0}. \quad (\text{H3})$$

### Appendix I: Calculation of the minimum achievable temperature

Here, we briefly calculate the theoretical performance limits of our setup. In particular, we are interested in the minimum achievable temperature(s). For strong feedback signals, following [16], we estimate the minimum temperature as

$$T_q^{\text{min}} = 2 \sqrt{T_0 \gamma \frac{\pi m}{2k_B} \Omega_q^2 S_{\text{imp},q}^{\ell,m}}. \quad (\text{I1})$$

For the results discussed here, where are limited to pressures on the order of  $5 \times 10^{-5}$  mbar, this implies  $(T_x^{\text{min}}, T_y^{\text{min}}, T_z^{\text{min}}) = (3.7, 29, 2.8) \pm (0.6, 4, 0.4)$  mK. Note that the pressure dependence of these values is encoded in the natural damping rate,  $\gamma$ , of the nanoparticle's motion.

### Appendix J: Influence of polarisation on demultiplexing performance

Here we show the effect that varying the polarisation of the trapping beam has on the demultiplexing performance. We find that there are specific linear polarisations where optimal demultiplexing is observed. That is, where each channel is primarily coupled to the inelastically scattered electric field generated by a unique translational degree of freedom  $q(t)$  for  $q = x, y$  and  $z$ . From the experimental results shown below, we find that the optimal case occurs for horizontally ( $\hat{e}_x$ ) and vertically ( $\hat{e}_y$ ) polarised trapping beams. Interestingly, we find that depending on the choice of polarisation,  $x(t)$  and  $y(t)$  are detected in alternating LP<sub>11a/b</sub> channels. Conversely, the LP<sub>01</sub> channel is consistently coupled to  $z(t)$ , with only minor contributions from the spectrally adjacent mode. This is shown in Fig 6 below, and agrees with those results shown in Fig. 2(a) of the main text.

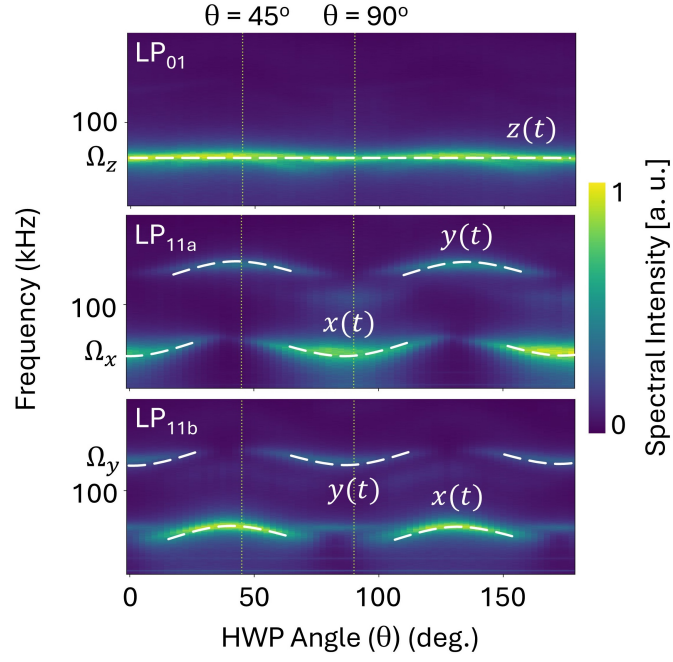


FIG. 6. The demultiplexing observed in each output channel of the spatial mode sorter as the polarisation ( $\theta$ ) of the trapping beam is varied using a half waveplate (HWP), leading to modifications in the electric field profile of the inelastically scattered field components. Here,  $\theta = 0^\circ$  refers to a horizontally polarised trapping beam ( $\hat{e}_x$ ) and  $\theta = 45^\circ$  to a vertically polarised trapping beam polarised ( $\hat{e}_y$ ), respectively.